JOURNAL OF THERMOPHYSICS AND HEAT TRANSFER
Vol. 19, No. 4, October–December 2005

Enhanced Heat-Source Cooling by Flow Pulsation and Porous Block

Po-Chuan Huang,* Shy-Her Nian,† and Chao-Fu Yang†
National Taipei University of Technology, Taipei 106, Taiwan, Republic of China

A numerical study has been carried out for forced pulsating flow in a parallel-plate channel with a porous-block-attached strip heat source at the bottom wall. Both the transient non-Darcy flow model taking the effects of the impermeable boundary, inertia, as well as variable porosity into consideration for the momentum equation and local thermal equilibrium model with thermal dispersion for energy transport were employed inside the porous region. Through the use of a stream function-vorticity transformation, the solution of the coupled governing equations for the porous/fluid composite system is obtained using the control-volume method. Comprehensive time-dependent flow and temperature data are calculated and averaged over a pulsation cycle in a periodic steady state. The effects of the important governing parameters, such as the particle diameter, the blockage ratio, pulsation frequency, and pulsation amplitude on the flow behavior in the vicinity of the porous block and the heat transfer rate from the heater are documented in detail. The results show that the cycle-space averaged Nusselt number for pulsating flow is higher than that for steady flow. The heat transfer enhancement factor increases with the increase of particle diameter, pulsation frequent, and blockage ratio, but decreases with the increase of pulsation amplitude. The method combining flow pulsation with a particle-porous heat sink can be considered as an augment heat transfer tool for cooling high-speed electronic devices.

Nomenclature

A = oscillating amplitude of axial inlet velocity
a, b = coefficients in Eq. (1)
B = coefficient of stagnant conductivity, Eq. (4)
C_p = specific heat at constant pressure, J/kg · K
Da = Darcy number, K/R^2
d_p = particle diameter, m
F = function used in expressing inertia terms
f = dimensional forcing frequency, Hz
H_p = height of porous block, m
h = convective heat transfer coefficient, W/m^2 · K
K = permeability of porous medium, m^2
k = thermal conductivity, W/m · K
k_d = stagnant conductivity, W/m · K
k_{eff} = effective thermal conductivity of porous block, W/m · K
k_s = thermal conductivity of solid phase in porous block, W/m · K
k_t = thermal dispersion conductivity, W/m · K
L_i = length of channel upstream from porous block, m
L_o = length of channel downstream from porous block, m
L_t = total length of channel as shown in Fig. 1a, m
Nu_m = cycle-space average Nusselt number, Eq. (25)
Nu_x = cycle-averaged local Nusselt number, Eq. (24)
$Nu_{x,t}$ = local instantaneous Nusselt number, Eq. (23)
P = pressure, N/m^2
Pe = Pelect number, $u_o R/\alpha$
Pr = Prandtl number, ν/α
R = height of channel, m
Rc_{eff} = effective heat capacity ratio, $(\rho C_p)_{\mathrm{eff}}/(\rho C_p)_f$
Re = Reynolds number, $u_o R/\nu$
Sr = dimensionless pulsating frequent, Strouhal number, fR/u_o
T = temperature, K
t = time, s
u = x-component velocity, m/s
u_i = inlet pulsating velocity, m/s
u_o = cycle-averaged velocity of the inlet flow, m/s
$\boldsymbol{V}$ = velocity vector, m/s
v = y-component velocity, m/s
W = width of heat source, m
x, y = Cartesian coordinates, m
α = thermal diffusivity, $k/\rho C_{p,}$, m^2/s
α_{eff} = effective thermal diffusivity, $k_{\mathrm{eff}}/\rho_f C_{p,f}$, m^2/s
δ = boundary-layer thickness, m
ε = porosity of porous medium
ε_∞ = freestream porosity
λ_{eff} = effective thermal conductivity ratio, k_f/k_{eff}
λ_s = thermal conductivity ratio of fluid phase to solid phase in porous block, k_f/k_s
μ = dynamic viscosity, kg/m · s
ν = kinematic viscosity, m^2/s
ξ = vorticity
ρ = density, kg/m^3
τ = oscillatory period for a cycle
φ = stream function
ω = angular velocity, 1/s
$\langle\,\rangle$ = volume-averaged quantity

Subscripts

eff = effective
f = fluid
i = inlet
p = porous
s = nonpulsating component
x = local

Superscript

$*$ = dimensionless quantity

Introduction

CONSIDERABLE attention has been given lately to thermal control of electronic devices due to the requirement of keeping

---

Received 24 April 2004; revision received 4 February 2005; accepted for publication 5 February 2005.

*Assistant Professor, Department of Air-Conditioning and Refrigeration Engineering; pchuang@ntut.edu.tw.

†Graduate Student, Department of Air-Conditioning and Refrigerating Engineering.

the component operating temperature at or below a maximum allowable level. Studies have proven that a significant change in the design temperature can lead to a perceptible reduction in the reliability of the electronic components. Different highly effective cooling techniques have been used in the past to obtain heat transfer enhancement with a minimum of frictional losses, including the traditional methods of natural and forced convective cooling. One of the promising techniques is the application of a porous material. This is due to the high ratio of surface area to volume in the heat transfer process and the enhanced flow mixing, caused by the tortuous path of the porous matrix, in the thermal dispersion process.

There have been significantly increasing numbers of studies of thermal convection in fluid-saturated porous media in past decade because of the presence of porous media in diverse engineering applications, including thermal insulation, heat exchangers, electronic cooling, drying process, etc. Extensive investigations have been conducted on the forced convection flow through a channel fully or partially packed with a porous material. Koh and Colony[1] analyzed the cooling effectiveness for a porous material in a cooling passage. Kaviany[2] studied heat transfer in porous media bounded by two isothermal parallel plates in laminar forced convection. Huang and Vafai[3,4] numerically simulated a forced convection problem in an isothermal parallel-plate channel with a porous-block or cavity-block array. Their results showed that porous substrate can substantially enhance the thermal performance in a channel. Among these studies, the heat transfer of a fully/partially porous channel with discrete heated sources was of special interest due to its applications on the cooling of electronics. Kuo and Tien[5] studied forced convection in a porous channel with discrete heat sources on one wall. They reported a two to four times increase of heat transfer as compared to that of slug flow in a clear duct. Hadim and Bethancourt[6] investigated forced convection in a fully/partially porous channel containing discrete heat sources on the bottom wall. A significant increase in heat transfer rate was observed as the Darcy number was decreased, especially at the leading edge of each heat source. Fu et al.[7] dealt with heat transfer from a porous-block-mounted heat plate in a channel flow. The effects of flow inertia, variable porosity, and a solid boundary were included. They reported that for the blocked ratio $H_p^* = 0.5$, the thermal performances are enhanced by higher porosity and porous particle diameter. However, the result is the opposite for $H_p^* = 1$.

Recently, because of the demands of high-performance electronic systems, there has been a growing need to achieve further augmented heat transfer from the fully/partially porous channel flow. One such effort has been directed to exploring the use of a porous heat sink subjected to flow pulsation. Here, a pulsating flow, that is, an oscillating component added to the mean flow, within a channel, can enhance the axial transfer of energy due to the presence of an axial gradient in the fluid temperature.[8–10] This oscillation-induced axial heat transport can be two or three orders of magnitude larger than pure molecular heat conduction.[10] Pulsating flow is frequently encountered in natural systems (human respiratory and vascular systems) and engineering systems [exhaust and intake manifolds of internal combustion (IC) engines, regenerators, Stirling engines, etc]. However, studies of pulsating flow passing through porous media are relatively scarce and often incomplete. Kim et al.[11] simulated forced pulsating flow in a fully porous channel. Their results showed that the effect of pulsation on heat transfer between the channel wall and fluid is more pronounced in case of a small pulsating frequency and a large pulsating amplitude. Khodadadi[12] analyzed a fully developed oscillatory flow through a porous medium channel bounded by two impermeable parallel plates, showing that the velocity profiles exhibit maxima next to the wall. Paek et al.[13] treated experimentally pulsating flow through a porous duct. It was indicated that the heat transport from the porous material decreases as pulsating frequency decreases at given amplitude and is decreased when the pulsating amplitude is large (>1) enough to cause a backward flow. Fu et al.[14] conducted experimentally the heat transfer of a porous channel subjected to oscillating flow and found that the length-averaged Nusselt number for oscillating flow is higher than that for steady flow. Most of these studies are related to the aspect of forced-pulsation convection over the fully porous system; however, little is known about the problem combining forced pulsation in a fluid/porous composite system. Guo et al.[15] investigated the pulsating flow and heat transfer in a partially porous pipe and indicated that the maximum effective thermal diffusivity was gained by pulsating flow through a pipe partially filled with a porous medium, rather than the limiting case of no porous medium or the full filling of a porous medium. The main motivation of the present study is to determine the effects of both the heat transfer enhancement factors by flow pulsation and a spherical-bead porous block on the convective cooling of an electronic device.

This paper presents a numerical investigation of forced pulsating convection in a parallel-plate channel with a porous-block-mounted heat source. The analysis is based on the use of an unsteady Navier–Stokes equation in the fluid region and the transient non-Darcy flow model, which considers the channeling, inertial, and solid boundary effects in the porous region. As for thermal dispersion in the energy equation, the correlation equation by Hsu and Cheng[16] is adopted. In this study, the basic interaction phenomena between the porous substrate and the fluid region, as well as the methodology for enhancing the heat transfer rate of a strip heater in a channel, have been analyzed. Detailed numerical results are obtained to describe the effects of various governing parameters defined in the problem, such as the particle diameter of porous block, the frequency and the amplitude of pulsation, or the blockage ratio. In addition, the results are also compared with those obtained for a steady nonpulsating flow.

Mathematical Formulation

Consider a pulsating flow in a channel with an isolated, heated strip source at uniform temperature, as shown in Fig. 1a. The channel width and total length are R and L_t, respectively, and both channel walls are insulated. The width and temperature of heat source are W, which is equal to R, and T_w, respectively. A porous-block heat sink with height H_p and width W_p is mounted on the heat source. At the channel inlet, a pulsating flow u_i, where $u_i = u_o[1 + A\sin(\omega t)]$, is imposed with a uniform temperature T_i.

To simplify the problem, the following assumption are made:

1) The flowfield is unsteady, two-dimensional, single-phase, laminar, and incompressible.

2) The fluid properties are constant, and the effect of gravity is neglected.

3) The porous block is made of spherical particles, and is nondeformable and does not have any chemical reaction with the fluids. The effective viscosity of porous medium is equal to the viscosity of the fluid.

4) The geometric function F and the permeability K of porous medium are based on Ergun's experimental findings,[17]

$$F = \frac{1.75}{\sqrt{(150)\varepsilon^3}}, \qquad K = \frac{\varepsilon^3 d_p^2}{150(1-\varepsilon)^2}$$

$$\varepsilon = \varepsilon_\infty[1 + a\exp(-by/d_p)] \tag{1}$$

where a and b are empirical constants.

5) The effective thermal conductivity of porous medium k_{eff} emerges as a combination of the stagnant conductivity k_d and thermal dispersion conductivity k_t, that is,

$$k_{\text{eff}} = k_d + k_t \tag{2}$$

where the stagnant component is based on the experimental findings of Zehner and Schlünder,[18] as follows:

$$\frac{k_d}{k_f} = \left[1 - (1-\varepsilon)^{\frac{1}{2}}\right] - \frac{2(1-\varepsilon)^{\frac{1}{2}}}{1-\lambda_s B}\left[\frac{(1-\lambda_s)B}{(1-\lambda_s B)^2}\,\ln(\lambda_s B) + \frac{B+1}{2} + \frac{B-1}{1-\lambda_s B}\right] \tag{3}$$

with

$$B = 1.25\left(\frac{1-\varepsilon}{\varepsilon}\right)^{10/9}, \qquad \lambda_s = \frac{k_f}{k_s} \tag{4}$$

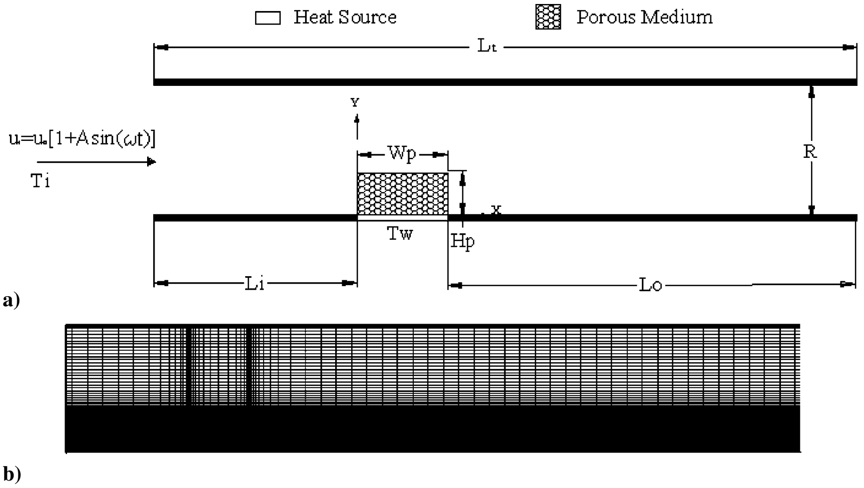

Fig. 1 Present configuration: a) schematic diagram and corresponding coordinate systems and b) typical nonuniform grid system for the whole computational domain.

The dispersion conductivity is determined based on experimental correlation reported by Hsu and Cheng,[16] given by

$$k_t = 0.04\left(\frac{1-\varepsilon}{\varepsilon}\right)\rho C_p u d \tag{5}$$

With the preceding assumptions, the governing conservation equations for the present problem can then be separately written for the porous and fluid regions. Treating the fluid-saturated porous medium as a continuum, the local averages of the conservation equations for mass, momentum, and energy in the porous region are[19]

$$\nabla\cdot\langle V\rangle = 0 \tag{6}$$

$$\left[\frac{1}{\varepsilon}\frac{\partial\langle V\rangle}{\partial t} + \frac{1}{\varepsilon^2}\langle(V\cdot\nabla)V\rangle\right] = -\frac{1}{\rho_f}\nabla\langle p\rangle^f + \left(\frac{\nu_f}{\varepsilon}\right)\nabla^2\langle V\rangle - \frac{\nu_f}{K}\langle V\rangle - \frac{F}{\sqrt{K}}[\langle V\rangle\cdot\langle V\rangle]J \tag{7}$$

$$\left\{(\rho C_p)_{\text{eff}}\frac{\partial\langle T\rangle}{\partial t} + (\rho C_p)_f[\langle V\rangle\cdot\nabla\langle T\rangle]\right\} = \nabla\cdot[K_{\text{eff}}\nabla\langle T\rangle] \tag{8}$$

The conservation equations for mass, momentum, and energy in the fluid region are

$$\nabla\cdot V = 0 \tag{9}$$

$$\frac{\partial V}{\partial t} + V\cdot\nabla V = -\frac{1}{\rho_f}\nabla P + \nu_f\nabla^2 V \tag{10}$$

$$\frac{\partial T}{\partial t} + V\cdot\nabla T = \alpha_f\nabla^2 T \tag{11}$$

The associated initial and boundary conditions necessary to complete the formulation of the problem are as follows. The unidirectional, pulsating flow at the channel inlet is given

$$x = 0, \qquad 0 < y < R, \qquad \text{for} \qquad t > 0$$

$$u_i = u_0[1 + A\sin(2\pi f t)], \qquad v = 0, \qquad T = T_i \tag{12a}$$

At the exit, the fully developed condition is satisfied

$$\frac{\partial u}{\partial x} = 0, \qquad \frac{\partial v}{\partial x} = 0, \qquad \frac{\partial T}{\partial x} = 0$$

$$\text{for} \qquad x = L_t, \qquad 0 < y < R \qquad \text{for} \qquad t > 0 \tag{12b}$$

The no-slip conditions at the perfectly insulated channel walls are

$$u = 0, \qquad v = 0, \qquad \frac{\partial T}{\partial y} = 0$$

$$\text{at} \quad \begin{cases} 0 < x < L_t, & & y = R \quad \text{for} \quad t > 0 \\ x < L_i, & L_i + W_p < x < L_t, & y = 0 \quad \text{for} \quad t > 0 \end{cases} \tag{12c}$$

At the wall of heat source, $L_i < x < L_i + W_p$, $y = 0$, for $t > 0$,

$$u = 0, \qquad v = 0, \qquad T = T_w \tag{12d}$$

Along the fluid/porous interface, the continuities of the velocity, pressure, stress, temperature, and heat flux are satisfied.[3]

When the stream function φ and vorticity ζ are introduced as

$$u = \langle u\rangle = \frac{\partial\varphi}{\partial y}, \qquad v = \langle v\rangle = -\frac{\partial\varphi}{\partial x}$$

$$\zeta = \frac{\partial v}{\partial x} - \frac{\partial u}{\partial y} = \frac{\partial\langle v\rangle}{\partial x} - \frac{\partial\langle u\rangle}{\partial y} \tag{13}$$

and the following dimensionless variables are introduced as

$$x^* = x/R, \qquad y^* = y/R, \qquad u^* = u/u_o, \qquad v^* = v/u_o$$

$$d_p^* = d_p/R, \qquad W_p^* = W_p/R, \qquad H_p^* = H_p/R \tag{14a}$$

$$Sr = fR/u_o, \qquad T^* = (T - T_i)/(T_w - T_i), \qquad t^* = tu_o/R$$

$$\varphi^* = \varphi/u_i R, \qquad \zeta^* = R\zeta/u_i \tag{14b}$$

then the foregoing two sets of conservation equations are transformed into one set of dimensionless stream function-vorticity formulation, which is valid throughout the composite system, as follows:

$$\varepsilon\frac{\partial\zeta^*}{\partial t^*} + u^*\frac{\partial\zeta^*}{\partial x^*} + v^*\frac{\partial\zeta^*}{\partial y^*} = \frac{\varepsilon}{Re}\nabla^2\zeta^* + S^* \tag{15}$$

$$\nabla^2\varphi^* = -\zeta^* \tag{16}$$

$$Rc\frac{\partial T^*}{\partial t^*} + u^*\frac{\partial T^*}{\partial x^*} + v^*\frac{\partial T^*}{\partial y^*} = \nabla\left(\frac{1}{\lambda Pe}\nabla T^*\right) \tag{17}$$

The dimensionless parameters in Eqs. (15–17) are Reynolds number Re, the heat capacity ratio Rc, the thermal conductivity ratio λ, and the Pelect number Pe. S^* is the source term. Then, the nondimensional parameters in the fluid region are

$$Rc_f = 1, \qquad Re_f = u_o R/\nu_f, \qquad Pe_f = u_o R/\alpha_f$$

$$\lambda_f = k_f/k_f = 1, \qquad S^* = 0, \qquad \varepsilon = 1 \tag{18}$$

In the porous region, the nondimensional parameters are

$$Rc_{\text{eff}} = (\rho C_p)_{\text{eff}}/(\rho C_p)_f, \qquad Re_{\text{eff}} = u_o R/\nu_{\text{eff}}$$

$$Pe_{\text{eff}} = u_o R/\alpha_{\text{eff}}, \qquad \lambda_{\text{eff}} = k_f/k_{\text{eff}} \tag{19}$$

$$S^* = -\frac{\varepsilon^2}{ReDa}\zeta_p^* - \frac{F\varepsilon^2}{\sqrt{Da}}\left|\boldsymbol{V}_p^*\right|\zeta_p^* - \frac{F\varepsilon^2}{\sqrt{Da}}\left[v_p^*\frac{\partial\left|\boldsymbol{V}_p^*\right|}{\partial x^*} - u_p^*\frac{\partial\left|\boldsymbol{V}_p^*\right|}{\partial y^*}\right]$$

$$-2\frac{v^*}{\varepsilon}\frac{\partial v^*}{\partial x^*}\frac{\partial\varepsilon}{\partial y^*} + \frac{u^*\varepsilon}{Re}\frac{\partial}{\partial y^*}\left(\frac{\varepsilon}{Da}\right) + u^*\varepsilon\left|\boldsymbol{V}_p^*\right|\frac{\partial}{\partial y^*}\left(\frac{F\varepsilon}{\sqrt{Da}}\right)$$

$$+u^*v^*\varepsilon\left[\frac{2}{\varepsilon^2}\left(\frac{\partial\varepsilon}{\partial y^*}\right)^2 - \frac{1}{\varepsilon^2}\frac{\partial^2\varepsilon}{\partial y^{*2}}\right] + \frac{v^*}{\varepsilon}\frac{\partial\varepsilon}{\partial y^*}\frac{\partial u^*}{\partial y^*} + \frac{u^*}{\varepsilon}\frac{\partial\varepsilon}{\partial y^*}\frac{\partial v^*}{\partial y^*}$$

$$+\frac{1}{\varepsilon}\frac{\partial\varepsilon}{\partial y^*}\left(\varepsilon\frac{\partial u^*}{\partial t^*} + u^*\frac{\partial u^*}{\partial x^*} + v^*\frac{\partial u^*}{\partial y^*}\right) \tag{20}$$

where the Darcy number, $Da = K/R^2$, is related to the permeability of the porous medium, which is proportional to the square of the nondimensional particle diameter [as seen from Eq. (1)].

The corresponding dimensionless boundary conditions, thus, become

$$\varphi^* = y^*, \qquad \xi^* = 0, \qquad T^* = 0, \qquad u^* = 1 + A\sin(2\pi Srt^*)$$

$$v^* = 0 \qquad \text{at} \qquad x^* = 0, \qquad 0 < y^* < 1, \qquad t^* > 0 \tag{21a}$$

$$\frac{\partial\varphi^*}{\partial x^*} = 0, \qquad \frac{\partial\xi^*}{\partial x^*} = 0, \qquad \frac{\partial T^*}{\partial y^*} = 0$$

$$\text{at} \qquad x^* = L_t^*, \qquad 0 < y^* < 1, \qquad t^* > 0 \tag{21b}$$

$$\varphi^* = 0, \qquad \xi^* = -\frac{\partial^2\varphi^*}{\partial y^{*2}}, \qquad \frac{\partial T^*}{\partial y^*} = 0, \qquad u^* = 0$$

$$v^* = 0 \qquad \text{at} \qquad 0 < x^* < L_t^*, \qquad y^* = 0, \qquad t^* > 0 \tag{21c}$$

$$\varphi^* = 1, \qquad \xi^* = -\frac{\partial^2\varphi^*}{\partial y^{*2}}, \qquad \frac{\partial T^*}{\partial y^*} = 0, \qquad u^* = 0$$

$$v^* = 0 \qquad \text{at} \qquad 0 < x^* < L_t^*, \qquad y^* = 1, \qquad t^* > 0 \tag{21d}$$

$$\varphi^* = 0, \qquad \zeta^* = -\frac{\partial^2\varphi^*}{\partial y^{*2}}, \qquad T^* = 1, \qquad u^* = 0$$

$$v^* = 0 \qquad \text{at} \qquad L_i^* < x^* < L_i^* + W_p^*, \qquad y^* = 0, \qquad t^* > 0 \tag{21e}$$

where $Sr = fR/u_o$ is the dimensionless pulsating frequency parameter (Strouhal number), and along the fluid/porous interface

$$u_p^*\big|_{g(x,y)=0} = u_f^*\big|_{g(x,y)=0}, \qquad v_p^*\big|_{g(x,y)=0} = v_f^*\big|_{g(x,y)=0}$$

$$\mu_{\text{eff}}\frac{\partial v_p^*}{\partial n^*}\bigg|_{g(x,y)=0} = \mu_f\frac{\partial v_f^*}{\partial n^*}\bigg|_{g(x,y)=0} \tag{22a}$$

$$\mu_{\text{eff}}\left[\frac{\partial u_p^*}{\partial n^*} + \frac{\partial v_p^*}{\partial t^*}\right]\bigg|_{g(x,y)=0} = \mu_f\left[\frac{\partial u_f^*}{\partial n^*} + \frac{\partial v_f^*}{\partial t^*}\right]\bigg|_{g(x,y)=0} \tag{22b}$$

$$T_P^*\big|_{g(x,y)=0} = T_f^*\big|_{g(x,y)=0}, \qquad k_{\text{eff}}\frac{\partial T_P^*}{\partial n^*}\bigg|_{g(x,y)=0} = k_f\frac{\partial T_f^*}{\partial n^*}\bigg|_{g(x,y)=0} \tag{22c}$$

where $g(x, y) = 0$ are the curves defining the porous/fluid interfaces and the derivative with respect to n and t represents the normal and tangential gradients, respectively, to these curves at any point on the interfaces.

To assess the effects of both flow pulsation and a porous block on the heat transfer rate at the heat source, the local instantaneous Nusselt number along the surface of the heat source is evaluated as

$$Nu_{x,t} = \frac{h(x,t)R}{k_f} = -\frac{k_{\text{eff}}}{k_f}\frac{\partial T^*}{\partial y^*}\bigg|_{y^*=0} \tag{23}$$

Then the corresponding local Nusselt number in a time average over one cycle of pulsation is calculated as

$$Nu_x = \frac{1}{\tau}\int_0^\tau Nu_{x,t}\,\mathrm{d}t \tag{24}$$

and the cycle-space averaged Nusselt number over a heat source

$$Nu_m = \frac{1}{\tau W}\int_0^\tau\int_0^w Nu_{x,t}\,\mathrm{d}x\,\mathrm{d}t \tag{25}$$

where W is the overall exposed length of heat source.

Numerical Method and Procedure

To obtain the solution of foregoing system of equations, the region of interest is overlaid with a variable grid system as shown in Fig. 1b. When the first-order fully implicit scheme for the time derivatives, the central differencing for the diffusion terms, and the second upwind differencing for the convective terms are applied, the transient finite difference form of the vorticity transport, the stream function, and the energy equations were derived by control-volume integration of these differential equations over discrete cells surrounding mesh points. The transient finite difference equations were solved by the extrapolated Jacobi scheme. This iterative scheme is based on a double cyclic routine, which translates into a sweep of only one-half of the grid points at each iteration step.[20] In this work, convergence was considered to have been achieved when the absolute value of relative error on each mesh point between two successive iterations was found to be less than 10^{-6}. Also, The steady nonpulsating flow results were used as the initial-state conditions to reduce the computational time. In most cases, steady periodic solutions were obtained after 15–45 cycles of pulsation. The time resolution was such that one pulsating period was divided into 60 time steps during the early 5–10 cycles and into 120 time steps for later cycles.

In addition, to ensure continuity of the convective and diffusive fluxes across the porous/fluid interface, the harmonic mean formulation suggested by Patankar[21] was used to handle abrupt variations in the thermophysical properties, such as the permeability, inertia factor, and thermal conductivity, across the interface.

A nonuniform spatial grid system with a large concentration of nodes in regions of steep gradients, such as those close to the wall and the porous-cover heater, was employed to obtain accurate vorticity, streamline, and isotherm distribution. Figure 1b shows a nonuniform grid system for the computational domain. A grid independence test showed that there is only a very small difference (less than 1%) in the space–time averaged Nusselt number among the solution for (160 × 57), (270 × 95), (210 × 142), and (514 × 70) grid distribution. Also, the time step was reduced until a further reduction did not significantly affect the results on amplitude and frequency. Therefore, a 270 × 95 grid system was adopted for the present work. In addition, special attention was given to the spatial mesh points in the boundary layer because the boundary-layer thickness δ/R for the classical oscillatory flow on a flat plate can be estimated as follows[22]:

$$\delta \sim (2\nu/\omega)^{\frac{1}{2}}, \qquad \delta/R \sim 1/(SrRe)^{\frac{1}{2}} \tag{26}$$

Thus, the dimensionless boundary-layer thickness becomes smaller as Strouhal and/or Reynolds number increases. Spatial grids were clustered to resolve the region of this thin boundary layer for high-frequency pulsation.

To validate the numerical scheme used in the present study, comparisons with three relevant results were made. This was achieved by making the necessary adjustments of our model to reduce it to a system equivalent to the simplified available cases. The relevant studies for our case correspond to the problems of 1) a two-dimensional

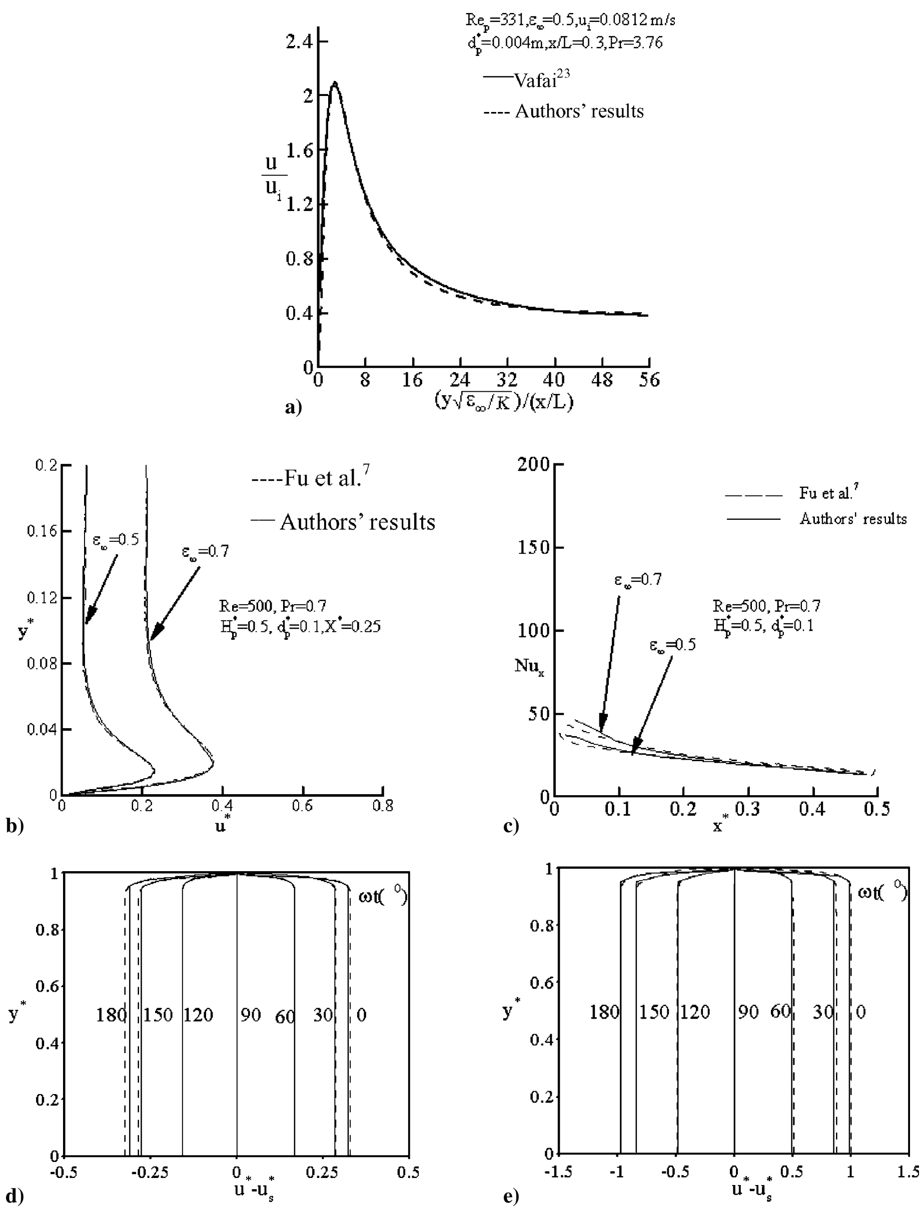

Fig. 2 Results compared with other literature: a) u^* velocity profiles with channel effect compared with those of Vafai,[23] b) and c) u^* velocity profiles near wall region and Nu_x distribution compared with those of Fu et al.,[7] and d) and e) profiles of time-dependent fluctuation of u^* compared with those of Kim et al.[11] for $Sr = 0.006$ and 0.16, respectively.

steady flow through a variable-porosity medium confined by an external boundary, that is, $H_p^* \to \infty$, $W_p^* \to \infty$, and $A = 0$; 2) a two-dimensional fully developed steady flow through a porous block mounted on a heated plate in a channel, that is, $H_p^* = 0.5$, $W_p^* = 0.5$, and $A = 0$, representing the nonpulsating steady case; and 3) forced pulsating flow in a channel filled with fluid-saturated porous media, that is, $H_p^* = 1$, and $W_p^* \to \infty$. The result for the first case was to compare the present numerical solution with the analytical solution of Vafai[23] for u/u_c velocity profiles at $Re_p = u_0 d_p/\nu_f = 331$, $d_p = 0.004$ m, $\varepsilon_\infty = 0.5$, $a = 0.98$, $b = 2$, and $x/L = 0.5$. Figure 2a shows the comparisons between the analytical solution of Vafai[23] and the present numerical solution for u^* velocity profiles at the aforementioned operating condition. The deviation of the maximum velocity is about 0.7%. For the second case, the results agree to better than 1% with data reported by Fu et al.[7] for u^* velocity profiles near the heated plate region at $x^* = 0.25$ and local Nusselt number Nu_x distributions along that heated surface, as shown in Figs. 2b and 2c, at $Re = 500$, $Pr = 0.7$, $d_p^* = 0.1$, and $x^* = 0.25$, for $\varepsilon_\infty = 0.5$ ($a = 0.98$ and $b = 2$) and 0.8 ($a = 0.42$ and $b = 2$). The third validity was to compare with the study of Kim et al.[11] for $Da = 10^{-4}$, $Re = 50$, $Pr = 0.7$, ε (constant porosity) $= 0.6$, $A = 0.75$, $Sr = 0.006$, and 0.16. Comparisons between the profiles of normalized time-dependent fluctuation $u_{t\_s}^* = u_t^* - u_s^*$ of velocity u^* calculated in Ref. 11 and the current analysis show discrepancies of less than 1.5% as shown in Figs. 2d and 2e.

Results and Discussion

The fixed input parameters utilized in the simulation were $L_i^* = 4$, $L_o^* = 10$, $Re = 500$, $Pr = 0.7$ (where the air is used as the cooling fluid, $k_f = 0.0267$ W/m K), $\varepsilon_\infty = 0.7$ [empirical constants in Eq. (1), $a = 0.98$ and $b = 2$], $Rc_{\text{eff}} = 1$, and $W_p^* = 1$. The porous material of the spherical bead adopted here is considered as having the same properties as copper ($k_s = 401$ W/m K). In this study, emphasis is placed on the effects of particle diameter ($0.05 < d_p^* < 0.2$), pulsation frequency ($0.1 < Sr < 0.5$), pulsation amplitude ($0.1 < A < 0.5$), and the blockage ratio ($0.3 < H_p^* < 0.5$) on the flow and heat transfer characteristics. Note that to illustrate the results of the flow and temperature fields near the porous-block-mounted strip heat source clearly, only this region and its vicinity were presented. However, at all times, the much larger domain was used for numerical calculations and interpretation of the results. In

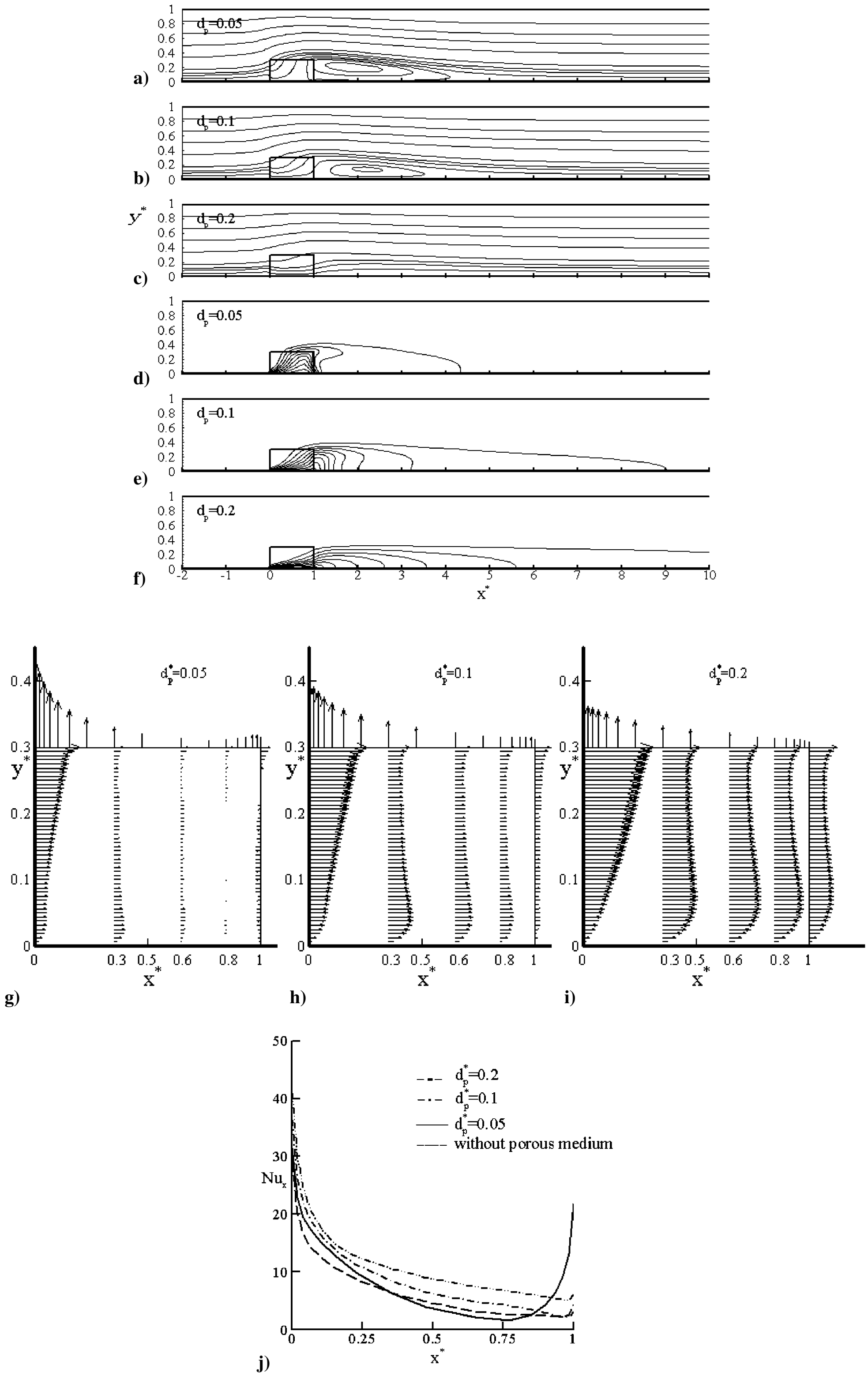

Fig. 3 Effects of the particle diameter on streamlines a)–c), isotherms d)–f), velocity distributions g)–i), and local Nusselt number distribution j) for a steady nonpulsating flow.

addition, for the sake of brevity, the main features and characteristics of some of the results are discussed and the corresponding figures are not presented.

Steady Flow

For comparison purposes, the typical velocity and temperature fields and the local Nusselt number distribution in the case of a steady nonpulsating flow ($A = 0$) are presented in the Fig. 3 with $Re = 500$, $Pr = 0.7$, $\varepsilon_\infty = 0.7$, $H_p^* = 0.3$, and $W_p^* = 1.0$, at three different particle diameters $d_p^* = 0.05$, 0.1, and 0.2. Note from Fig. 3a that, for smaller $d_p^* = 0.05$, the streamlines inside the porous block move upward and a recirculation zone is formed behind the porous block. The mechanism for the formation of this complicated flowfield within the channel is the consolidated result of four effects: 1) a penetrating effect pertaining to the porous medium, 2) a blowing effect caused by porous media displacing transversely the fluid from the porous region into the fluid region, 3) a suction effect caused by the pressure drop behind the porous blocks resulting in a reattached flow, and 4) the effects of boundary-layer separation. The temperature field corresponding to the preceding flowfield is displayed in Fig. 3d. On the top interface of the porous block, the isotherms spread upward due to the blowing effect, whereas on the rear interfacial surface, the isotherms are crowded upwind due to the neighboring clockwise-rotating recirculation effect. The variation of local Nusselt number along the heat source plate is illustrated in Fig. 3j. A large local Nusselt number occurs at the leading edge of the heat source where the thermal boundary layer begins to grow, and then the Nusselt number declines to a local minimum value due to boundary-layer growth. Near the right corner of heat source, Nu_x increases quickly again. This is because the boundary-layer separation occurs, resulting in an increase in the convective energy transport caused by the fluid eddy mixing. Note that the aforementioned enhanced heat transfer effect caused by vertex convection occurs only when the recirculation zone penetrates the porous block.

The effect of particle diameter d_p^* is also shown in Fig. 3. Figure 3 shows that as d_p^* increases the mass flow rate passing directly through the porous block increases and the downstream recirculation zone becomes small and finally disappears, as indicated in Figs. 3a–3c. This is due to the smaller drag force that the flow encounters at larger value of d_p^* under the same porosity condition. This, in turn, causes a smaller blowing effect through the porous block, which confines the development of downstream recirculation zone. In addition, increasing d_p^* causes the channel effect to be more pronounced (Figs. 3g–3i). The higher velocity exists near the solid wall (heat source surface). This result was also found in the work of Fu et al.[7] These higher velocities can increase the convected energy and form a thinner thermal boundary layer inside the porous region (Figs. 3d–3f) which leads to higher values of local Nusselt number distribution, as illustrated in Fig. 3j, except in the rear part of the porous block where the recirculation zone appears. Comparison of the Nu_x distribution for the heat source with and without a porous block shows that, for larger d_p^* (>0.1), the heat transfer is enhanced along the whole heat source due to the channeling effect observed throughout the heater surface.

Pulsating Flow

The aforementioned stable and steady flow structures can be destabilized by inducing pulsation, which results in the strong interaction of the bulk fluid flow with the boundary layer and, thus, enhances thermal transport. The influence of pulsation is now explained. Figure 4a shows the flow patterns over one pulsating cycle at a periodic steady state for $Re = 500$, $Pr = 0.7$, $d_p^* = 0.05$, $Sr = 0.1$, $A = 0.5$, $\varepsilon_\infty = 0.7$, $W_p^* = 1.0$, $H_p^* = 0.3$, $L_i^* = 4$, and $L_o^* = 10$, with six successive phase angle of $\omega t = 0, \pi/3, 2\pi/3, \pi, 4\pi/3$, and $5\pi/3$. In Fig. 5a, the u^* is plotted as a function of time at a monitoring point ($x = L_i + W_p - 0.5$, $y = H_p/2$). The x-component velocity exhibits a time-asymptotic periodic-steady behavior after about 40 cycles of pulsation. Figure 5b shows phase diagrams of u^* vs v^* at the same monitoring point. The Fig. 5b phase diagram displays a well-closed loop, which indicates that the flow is in a high time-periodic regime. Note in Fig. 4a that for smaller $d_p^* = 0.05$ two recirculating cells in both the upstream and downstream of the porous block shrink and expand cyclically as the result of forcing pulsation. This periodic alternation of flow structure contributes to the bulk mixing of fluids in the porous-block region. The interaction of recirculations with the core flow influences the temperature field if the downstream vortex zone deeply penetrates into the porous block. Figure 4b shows the impact of pulsation on the thermal field. Comparison of Fig. 4b with Fig. 3d indicates that the thermal field under a pulsating flow presents a periodic oscillation of the thermal boundary-layer thickness. The thermal boundary-layer thickness descends during the acceleration phase of the cycle ($\omega t = 0$ to $\pi/2$ and $3\pi/2$ to 2π) and rises during the deceleration phase of the cycle ($\omega t = \pi/2$ to $3\pi/2$). This is because when the flow velocity is low, the ratio of fluid residence time over the heat source plate to the heat diffusion time is high, allowing more heat to diffuse per unit of volumetric flow. This results in higher flow temperatures and a less steep temperature gradient at the wall. The depth of heat penetration into the fluid increases at those times. When the flow velocity is high, decreasing that ratio leads to lower flow temperatures and greater temperature gradients. In addition, the upstream and downstream recirculation zones cause the isotherms to extend upstream.

Effect of Particle Diameter

In the pulsation channel flow, the effect of particle diameter d_p^* of a porous medium is shown in Fig. 4 for the same flow condition at three different particle diameters, $d_p^* = 0.05$, 0.1, and 0.2, respectively. Comparison of the streamline variation shows that as d_p^* increases, the size and strength of the aforementioned recirculation zones become smaller or disappear at each time, and most of the fluid directly flows through the porous block due to the smaller drag force. The temperature fields are affected in a similar way. For larger d_p^*, the isotherms extend downstream more conspicuously, and the instantaneous thickness of thermal boundary layer becomes smaller. (For brevity, the corresponding figures are not presented here.) Figure 4c shows the variation of cycle-averaged local Nusselt number Nu_x with d_p^*. The values of Nu_x increase as d_p^* increases because of the larger oscillation temperature gradients near the heat source surface, except in the rear part of heater where the large vortex zone appears at $d_p^* = 0.05$. Comparison of the cycle-averaged local Nusselt number Nu_x distribution of pulsating and nonpulsating ($A = 0$) flows with the porous block case in Fig. 4c shows that the value of Nu_x for pulsating flow is higher than that for steady nonpulsating flow. This is caused by the larger cycle-averaged temperature gradients near the heat source surface. In addition, the larger the diameter, the larger the difference between the Nu_x of the pulsating and nonpulsating flows because cycle-averaged temperature gradients near the heat source surface are more pronounced, except in the front part of heater where the small vortex zone appears at $d_p^* = 0.05$.

To obtain an overall measure of heat transport characteristics in the present study, the influence of both flow pulsation and the porous-block heat sink on the heat transfer enhancement factors $Nu_m/(Nu_m)_{\text{non-}s}$ and $Nu_m/(Nu_m)_s$, which give the cycle-space averaged Nusselt number over a heat source normalized by the corresponding steady nonpulsation nonporous-block value $(Nu_m)_{\text{non-}s}$ and steady nonpulsating value $(Nu_m)_s$, respectively, is calculated. Figure 4d shows the effect of d_p^* on $Nu_m/(Nu_m)_{\text{non-}s}$ and $Nu_m/(Nu_m)_s$. It is clear from Fig. 4d that the gain in $Nu_m/(Nu_m)_s$ increases with increasing d_p^*. For $d_p^* = 0.2$, the cycle-space average Nusselt number of the pulsating flow is about 1.48 times that of the nonpulsating flow and about 1.95 times that of the nonpulsating flow over a nonporous-block heater.

Effect of Pulsating Frequency Strouhal Number

The effect of variations in the pulsating frequency or Strouhal number is shown in Fig. 6 for $Re = 500$, $Pr = 0.7$, $\varepsilon_\infty = 0.7$, $d_p^* = 0.1$, $A = 0.5$, $W_p^* = 1.0$, $H_p^* = 0.3$, $L_i = 4$, and $L_o = 10$ with $Sr = 0.1$, 0.3, and 0.5, respectively. The flowfields during a pulsating cycle with a phase angle increment of $\pi/3$ reveal that when the Strouhal number is larger, the recirculation zone behind the porous block becomes less pronounced at each time, and near the heat source surface more fluid with higher velocity flows directly through the porous block. This leads to a steep velocity gradient near the heat source plate, that is, a higher channel effect. The instantaneous thickness of the thermal boundary layers decreases with the increase of the pulsating frequency or Strouhal number (figures not presented). The reason for this trend is that an increasing Strouhal number causes heat penetration distance into the fluid and the oscillation of this depth during a cycle to decrease. The effects of Strouhal number on the cycle-averaged local Nusselt number distribution are shown in Fig. 6a. Note that an increase in Strouhal number results in an increase in Nu_x due to the larger oscillation temperature gradients in the direction normal to the heat source surface. This in turn increases the heat transfer rate from the heat source to the fluid. As expected, when Strouhal number increases, the gain in $Nu_m/(Nu_m)_s$ or $Nu_m/(Nu_m)_{\text{non-}s}$ increases as shown in Fig. 6b. The ratio values of $Nu_m/(Nu_m)_{\text{non-}s}$ are larger than those of $Nu_m/(Nu_m)_s$ because the value of $(Nu_m)_s$ is larger than that of $(Nu_m)_{\text{non-}s}$.

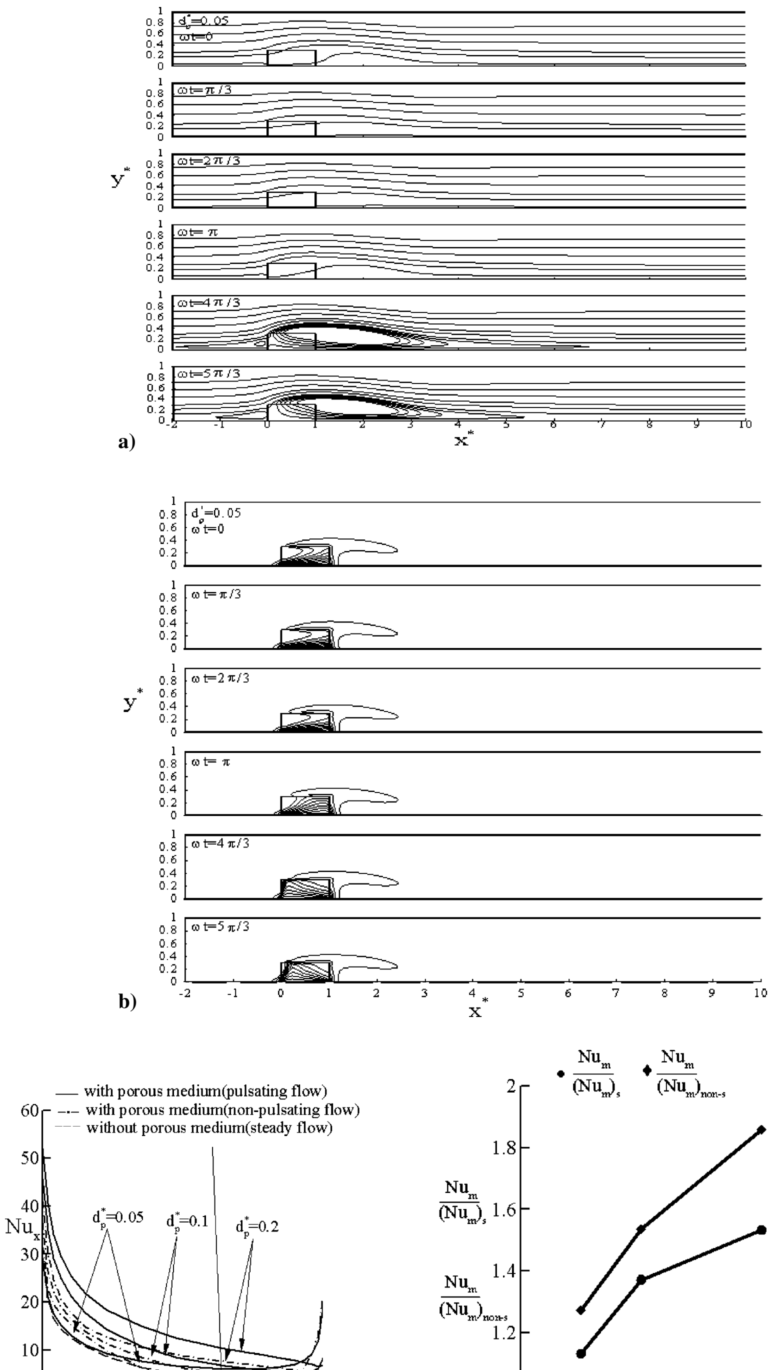

Fig. 4 Effects of particle diameter on the variations of a) streamlines ($\Delta\varphi^* = 0.2$ for $0 < \varphi^* < 1$), b) isotherms ($\Delta T^* = 0.1$), c) cycle-averaged Nusselt number, and d) heat transfer enhancement factor during a periodic-steady cycle.

Effect of Pulsating Amplitude A

Figure 7 shows the effect of A on the variation of Nu_x, $Nu_m/(Nu_m)_s$ and $Nu_m/(Nu_m)_{\text{non-}s}$ over a periodic-steady pulsating cycle for $Re = 500$, $Pr = 0.7$, $d_p^* = 0.1$, $Sr = 0.1$, $H_p^* = 0.3$, $W_p^* = 1.0$, $L_i^* = 4$, and $L_o^* = 10$ at $A = 0.1$, 0.3, and 0.5. Based on the inlet pulsating velocity in Eq. (12a), the larger the pulsating amplitude A is, the higher the flow deceleration becomes during the flow pulsation reversal ($\omega t = \pi$ to 2π). This leads to the production of the stronger downstream recirculation zones due to the lower flow momentum and the larger thickness of the temporal thermal boundary layer due to the relatively longer residence time of fluid over the heat source surface. It is seen from Fig. 7a that Nu_x decreases with increased A due to the smaller oscillation temperature gradients near the heat source surface. Note that for a larger pulsating amplitude such as $A = 0.5$, most of the area of the temporal recirculation zone is outside the porous block, which only has a slight assistance in the convective heat diffusion. Therefore, with an increase in A from 0.1 to 0.5, $Nu_m/(Nu_m)_s$ decreases from 1.57 to 1.53, and $Nu_m/(Nu_m)_{\text{non-}s}$ decreases from 1.46 to 1.43, as shown in Fig. 7b.

Effect of Porous Blockage Ratio H_p^*

Figure 8 shows the changes in Nu_x, $Nu_m/(Nu_m)_s$ and $Nu_m/(Nu_m)_{\text{non-}s}$ as H_p^* increases from 0.3 to 0.5 for $Re = 500$, $d_p^* = 0.1$, $Sr = 0.1$, $A = 0.5$, $W_p^* = 1.0$, $L_i^* = 4$, and $L_o^* = 10$. The flowfields (not shown) illustrate that the length and the relative weakness of the downstream recirculation zone increase with increasing H_p^* during the flow pulsating reversal, and more fluid flows through

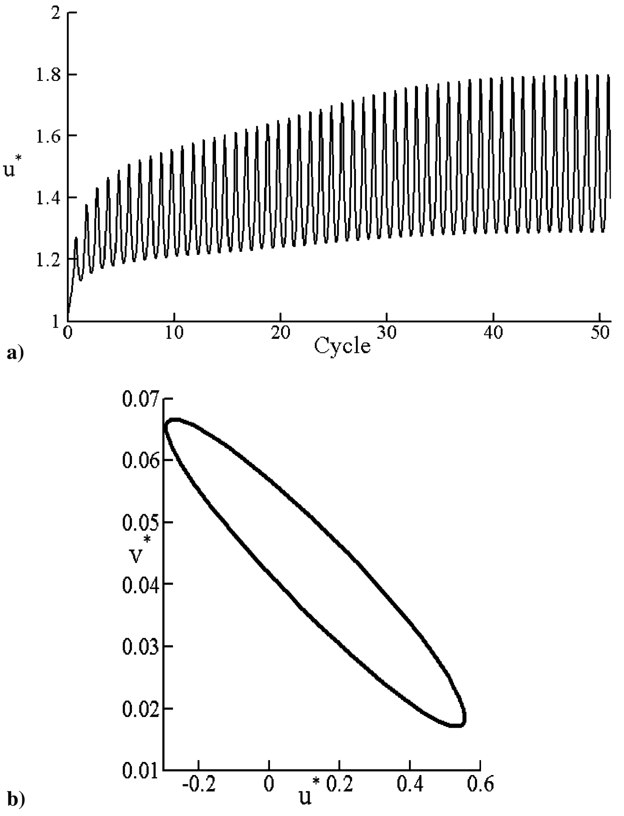

Fig. 5 For u^*: a) velocity u^* as a function of time and b) phase diagram of u^* vs v^* at $(x^*, y^*) = (L_i^* + W_p^* - 0.5$, and $H_p^*/2)$.

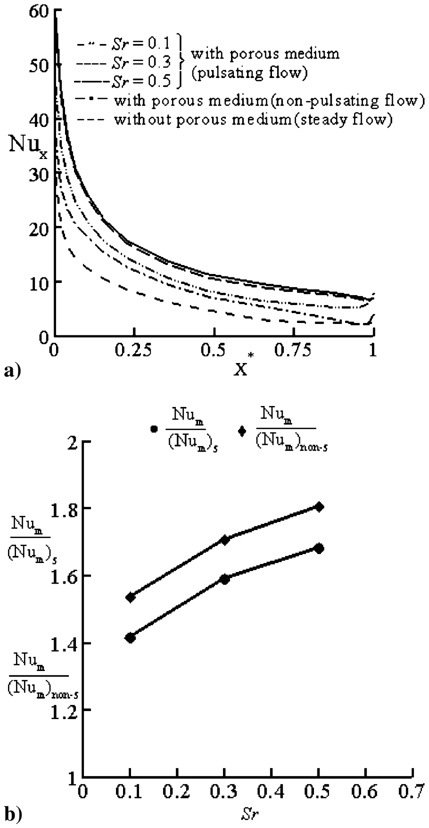

Fig. 6 Effect of pulsating frequency Strouhal number on a) cycle-averaged Nusselt number and b) heat transfer enhancement factor during periodic-steady cycle.

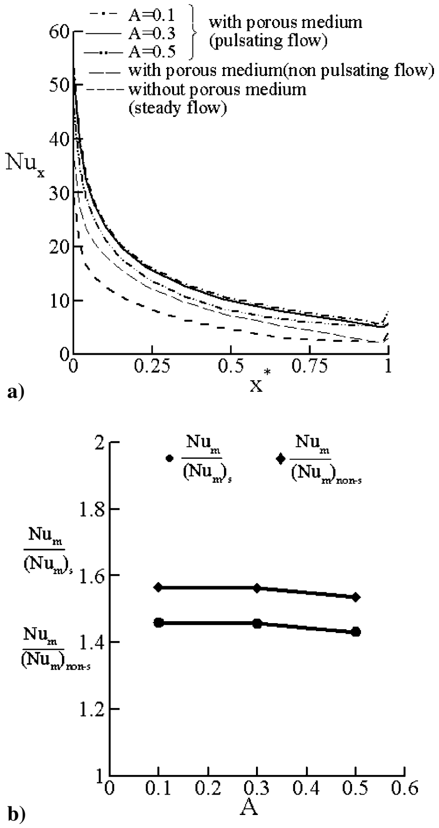

Fig. 7 Effect of pulsating amplitude on a) cycle-averaged Nusselt number and b) heat transfer enhancement factor during a periodic-steady cycle.

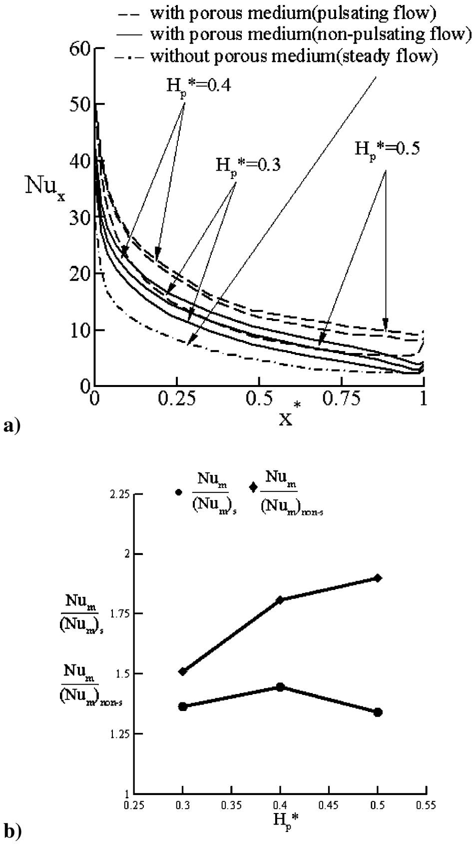

Fig. 8 Effect of the porous blockage ratio H_p^* on a) cycle-averaged Nusselt number and b) heat transfer enhancement factor during a periodic-steady cycle.

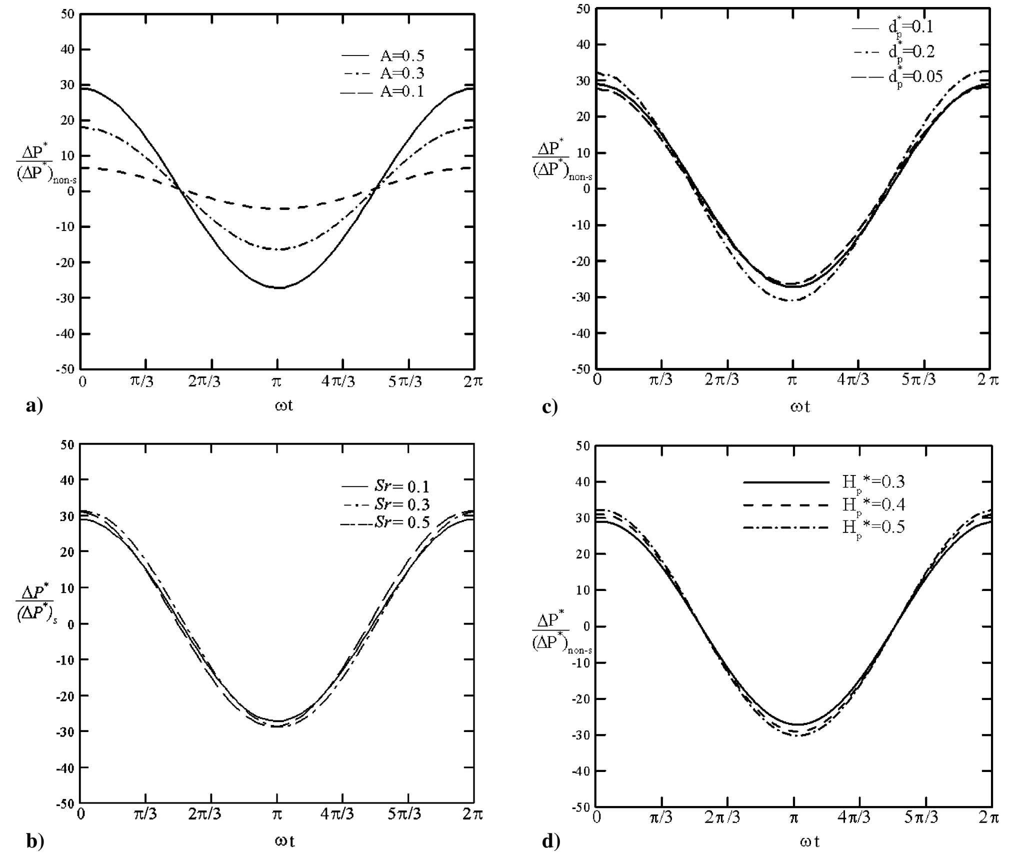

Fig. 9 Temporal variations of pressure drop factor along upper plate for various values of a) A, b) Sr, c) d_p^*, and d) H_p^*.

the porous block. In addition, the downstream recirculation zone moves away from the porous block. This is because of the relative increase in the height of the porous block, which, in turn, offers a higher degree of obstruction to the flow and accelerates the core flow to satisfy the mass continuity. This limits the development of the downstream recirculation zone in the transverse direction and leads to the recirculation zone moving outside of the porous block. Meanwhile, the isotherms with smaller instantaneous thermal boundary-layer thicknesses extend downstream more conspicuously at each time for the larger H_p^*. As expected, Nu_x increases with increasing H_p^*, shown in Fig. 8a, due to the existance of larger velocity near the heater surface. Therefore, the gain in $Nu_m/(Nu_m)_{\text{non-}s}$ is more substantial for larger H_p^*, shown in Fig. 8b.

Pressure Drop Calculation

When both porous material and flow pulsation for heat transfer augmentation are used, an important factor to consider is the penalty arising from increased pressure drop. In the stream function-vorticity formulation, the pressure field is eliminated in obtaining the solution. However, the pressure field can be recovered from the converged stream function and vorticity fields. This is done by integrating the pressure gradient along the upper channel wall. The temporal pressure gradient is derived from the unsteady momentum equation using the no-slip boundary conditions on the solid wall. The temporal pressure drop ΔP^* along the upper channel wall is then obtained from

$$\Delta P^* = \int_0^{L^*} \left.\frac{\partial P^*}{\partial x^*}\right|_{y^*=1} \mathrm{d}x^* = -\int_0^{L^*} \left.\left[\frac{\partial u^*}{\partial t^*} + \frac{1}{Re}\frac{\partial \xi^*}{\partial y^*}\right]\right|_{y^*=1} \mathrm{d}x^* \tag{27}$$

The corresponding steady nonpulsating ($A = 0$) nonporous-block pressure drop $(\Delta P^*)_{\text{non-}s}$ is

$$(\Delta P^*)_{\text{non-}s} = \int_0^{L^*} \left.\frac{\partial P^*}{\partial x^*}\right|_{y^*=1} \mathrm{d}x^* = -\int_0^{L^*} \left.\frac{1}{Re}\frac{\partial \xi^*}{\partial y^*}\right|_{y^*=1} \mathrm{d}x^* \tag{28}$$

where pressure P^* is nondimensionalized with respect to ρu_o^2. The effects of A, Strouhal number, d_p^*, and H_p^* on the temporal pressure drop factor $\Delta P^*/(\Delta P^*)_{\text{non-}s}$, which gives the overall pressure drop throughout the entire channel length, normalized by the corresponding steady nonpulsating nonporous-block value $(\Delta P^*)_{\text{non-}s}$, are presented in Fig. 9, respectively. In Fig. 9a, the amplitude of the temporal pressure drop factor increases substantially as A increases at $Re = 500$, $d_p^* = 0.1$, $Sr = 0.1$, $H_p^* = 0.3$, and $W_p^* = 1.0$. However, the magnitude of $\Delta P^*/(\Delta P^*)_{\text{non-}s}$, is not significantly affected by a change in Strouhal number (at $Re = 500$, $Sr = 0.1$, $A = 0.5$, $H_p^* = 0.3$, and $W_p^* = 1.0$), d_p^* (at $Re = 500$, $Sr = 0.1$, $A = 0.5$, $H_p^* = 0.3$, and $W_p^* = 1.0$), or H_p^* (at $Re = 500$, $d_p^* = 0.1$, $Sr = 0.1$, $A = 0.5$, and $W_p^* = 1.0$), as seen in Figs. 9b–9d. The required pumping power to maintain a pulsating flow increases with pulsation amplitude. The phase lead of $\Delta P^*/(\Delta P^*)_{\text{non-}s}$ over the inlet pulsating velocity for all cases studied here is around $\pi/2$. This indicates that the flow pulsation considered in this study is in a higher frequency regime compared to the oscillating flow inside a smooth duct.[22] In this classical oscillating flow, the phase lead of pressure drop over the inlet velocity approaches $\pi/2$ from zero as ω increases.

Conclusions

In this study, a numerical analysis was conducted to investigate the heat transfer characteristics on a porous-block-mounted heat source subjected to both steady and pulsating channel flow. The results can be summarized as follows:

1) For the nonpulsating steady flow case, the heat transfer rate from a strip heater could be enhanced by a copper porous block with higher particle diameter.

2) For the pulsating flow case, the stable and steady flowfield is significantly destabilized by introducing pulsation and exhibits a regularly expanding and shrinking alteration of the vortex structure. The phase diagram also shows that this unsteady pulsating flow is in a time-periodic regime. The thermal field is substantially affected in a similar way and presents a periodic oscillation of the thermal boundary-layer thickness near the heater surface.

3) The cycle-averaged local Nusselt number for pulsating flow is higher than that for nonpulsating steady flow. The heat transfer enhancement factor $Nu_m/(Nu_m)_{\text{non-}s}$ of the heater increases with increasing particle diameter, pulsation frequent, and porous blockage ratio, but decreases with increasing pulsation amplitude.

4) The results of this investigation indicate that a heat resource with a high-conductivity particle-porous block subjected to forced pulsating channel flow is a new and effective method for cooling electric devices. However, one must consider a tolerance limit in view of the increased pressure drop to determine the optimal amplitude of external pulsation according to the porous blockage ratio.

Acknowledgment

The first author gratefully acknowledges the support of the National Science Council of the Republic of China through Contract NSC 90-2212-E-027-012.

References

[1] Koh, J. C. Y., and Colony, R., "Analysis of Cooling Effectiveness for Porous Material in a Coolant Passage," *Journal of Heat Transfer*, Vol. 96, No. 1, 1974, pp. 324–330.

[2] Kaviany, M., "Laminar Flow through a Porous Channel Bounded by Isothermal Parallel Plate," *International Journal of Heat and Mass Transfer*, Vol. 28, No. 4, 1985, pp. 851–858.

[3] Huang, P. C., and Vafai, K., "Analysis of Forced Convection Enhancement in a Parallel Plate Using Porous Blocks," *Journal of Thermophysics and Heat Transfer*, Vol. 18, No. 3, 1994, pp. 563–573.

[4] Huang, P. C., and Vafai, K., "Internal Heat Transfer Augmentation in a Channel Using an Alternate Set of Porous Cavity-Block Obstacles," *Numerical Heat Transfer, Part A*, Vol. 25, No. 5, 1994, pp. 519–539.

[5] Kuo, S. M., and Tien, C. L., "Heat Transfer Augmentation in a Foam-Material Filled Duct with Discrete Heat Sources," Thermal Phenomena in Electronics Components Conf., Inst. of Electrical and Electronics Engineers, New York, 1988, pp. 87–91.

[6] Hadim, H. A., and Bethancourt, A., "Numerical Study of Forced Convection in a Partially Porous Channel with Discrete Heat Sources," *Journal of Electronic Packaging*, Vol. 117, No. 1, 1995, pp. 46–51.

[7] Fu, W. S., Huang, H. C., and Liou, W. Y., "Thermal Enhancement in Laminar Channel Flow with a Porous Block," *International Journal of Heat and Mass Transfer*, Vol. 39, No. 10, 1996, pp. 2165–2175.

[8] Chatwin, P. C., "On the Longitudinal Dispersion of Passive Contaminant in Oscillatory Flows in Tube," *Journal of Fluid Mechanics*, Vol. 71, 1975, pp. 513–527.

[9] Watson, E. J., "Diffusion in Oscillatory Pipe Flow," *Journal of Fluid Mechanics*, 1983, Vol. 133, pp. 233–244.

[10] Kurzweg, U. H., "Enhanced Heat Conduction in Oscillatory Viscous Flows Within Parallel-Plate Channels," *Journal of Fluid Mechanics*, Vol. 156, 1985, pp. 291–300.

[11] Kim, S. Y., Kang, B. H., and Hyun, J. M., "Heat Transfer from Pulsating Flow in Channel Filled with Porous Media," *International Journal of Heat and Mass Transfer*, Vol. 37, No. 14, 1994, pp. 2025–2033.

[12] Khodadadi, J. M., "Oscillatory Fluid Flow Through a Porous Medium Channel Bounded by Two Impermeable Parallel Plates," *Journal of Fluids Engineering*, Vol. 113, 1991, pp. 509–511.

[13] Paek, J. W., Kang, B. H., and Hyun, J. M., "Transient Cool-Down of a Porous Medium in Pulsating Flow," *International Journal of Heat and Mass Transfer*, Vol. 42, No. 18, 1999, pp. 3523–3527.

[14] Fu, H. L., Leong, K. C., and Liu, C. Y., "An Experimental Study of Heat Transfer of a Porous Channel Subjected to Oscillating Flow," *Journal of Heat Transfer*, Vol. 110, No. 1, 2001, pp. 946–954.

[15] Guo, Z., Kim, S. Y., and Sung, H. Y., "Pulsating Flow and Heat Transfer in a Pipe Partially Filled with a Porous Medium," *International Journal of Heat and Mass Transfer*, Vol. 40, No. 17, 1997, pp. 4209–4218.

[16] Hsu, C. T., and Cheng, P., "Thermal Dispersion in a Porous Medium," *International Journal of Heat and Mass Transfer*, Vol. 33, No. 8, 1990, pp. 1587–1597.

[17] Ergun, S., "Fluid Flow Through Packed Columns," *Chemical Engineering Progress*, Vol. 48, No. 2, 1952, pp. 89–94.

[18] Zehner, P., and Schlünder, E. U., "Thermal Conductivity of Granular Materials of Moderate Temperatures," *Chemie Ingenieur Technik*, Vol. 42, No. 14, 1970, pp. 941–993.

[19] Amiri, A., and Vafai, K., "Transient Analysis of Incompressible Flow Through a Packed Bed," *International Journal of Heat and Mass Transfer*, Vol. 41, No. 24, 1998, pp. 4259–4279.

[20] Adams, J., and Ortega, A. J., "A Multicolor SOR Method for Parallel Computation," *Proceedings of the International Conference on Parallel Procession*, IEEE Computer Society Press, Piscataway, NJ, 1982, pp. 53–56.

[21] Patankar, S. W., *Numerical Heat Transfer and Fluid Flow*, McGraw–Hill, New York, 1980, Chaps. 5 and 6, pp. 79–138.

[22] Schlichting, H., *Boundary-Layer Theory*, McGraw–Hill, New York, 1979, Chap. 15, pp. 408–448.

[23] Vafai, K., "Convection Flow and Heat Transfer in Variable-porous Media," *Journal of Fluid Mechanics*, Vol. 147, 1984, pp. 233–259.